PAPER

Check for updates

Exploring the feasibility of a two-dimensional layered cobalt-based coordination polymer for supercapacitor applications: effect of electrolytic cations†

Rakesh Deka,[a] Shashank Rathi[a] and Shaikh M. Mobin ⓘ [*abc]

Coordination polymers have attracted much interest in energy-related applications due to their adaptable structures and unique photophysical and chemical properties. In this study, a coordination polymer, **Co-CP**, was synthesized using a mixed ligand strategy *via* a slow diffusion technique. Single-crystal X-ray diffraction studies confirmed the characteristic two-dimensional structure of **Co-CP**, and plate-like morphology was authenticated through SEM images. **Co-CP** facilitates ion transport and efficient charge transfer processes, making it an ideal active material for supercapacitor applications. The results from the electrochemical studies demonstrate excellent supercapacitor properties for **Co-CP**, exhibiting a specific capacitance of 1092 F g^{-1} at 1.5 A g^{-1} in 7 M NaOH. Furthermore, the kinetic effect of the electrolyte cation was also investigated in a two-electrode asymmetric supercapacitor (ASC) system by preparing three different gels (NaOH-PVA, KOH-PVA, and LiOH-PVA). Similar trends were observed for the ASC device, with the highest energy density of 17 W h Kg^{-1} at a power density of 1200 W Kg^{-1} in NaOH-PVA gel. Overall, the results suggest that **Co-CP** is a promising active material for supercapacitor applications, and the choice of electrolyte cation has a remarkable impact on the electrochemical performance of the device. This study provides valuable insights for the development and optimization of high-performance supercapacitors based on coordination polymers.

Introduction

The high demand for energy and the requirement to reduce greenhouse gas emissions force the development of various energy storage technologies.[1] Energy storage systems play a crucial role in providing reliable and sustainable energy to meet the growing needs of modern society.[2,3] They are essential in balancing the mismatch between energy supply and demand, integrating sustainable energy sources into the grid, and improving the efficiency of energy systems.[4] In recent years, supercapacitors have gained tremendous interest as energy storage devices.[5,6] Contrary to batteries, they possess high capacitance and low internal resistance.[7] Moreover, they have a quick charge/discharge cycle, high power density, and cyclic retention.[8,9] Along with these characteristics, they also show an extensive thermal range that can reach up to −40 °C.[10]

Intriguing applications for supercapacitors include fuel cells and low-emission electric vehicles, but they are also widely employed in consumer electronics and medical technology.[11,12] Supercapacitors have been classified on the basis of physio-chemical processes accountable for the energy storage mechanism such as:[10,13] (1) electric double-layer capacitance (EDLC) and (2) pseudocapacitors. The electrodes of an EDLC are typically made of activated carbon, which has a very high surface area per unit volume, and charge storage occurs electrostatically. When voltage is applied across the electrodes, ions in the electrolyte solution travel to the surface of the carbon electrodes. This creates a double layer of charge, with the positive ions adsorbed on the negative electrode and the negative ions adsorbed on the positive electrode.[14] However, reversible redox reaction occurred through the faradaic process at the electrode–electrolyte junction for pseudocapacitors.[15–17] Owing to the faradaic process, the pseudocapacitor exhibits higher capacitance. Metal oxides such as Co_3O_4[18] and $Ni(OH)_2$[19] and conducting polymers (*e.g.*, polypyrrole[20]) are highly explored materials as pseudocapacitors.

Over the past few years, graphene and other 2D materials such as MXenes,[21,22] 2D covalent organic frameworks (COFs),[23] B_4C,[24] C_3N_4,[25] 2D coordination polymers (CPs)[26] and layered

[a] Department of Chemistry, India. E-mail: xray@iiti.ac.in; Tel: +91 731 6603 336
[b] Center for Electric Vehicle and Intelligent Transport System (CEVIT), India
[c] Center of Advanced Electronics (CAE), Indian Institute of Technology Indore, Khandwa Road, Simrol, Indore 453552, India

† Electronic supplementary information (ESI) available. CCDC 2285196. For ESI and crystallographic data in CIF or other electronic format see DOI: https://doi.org/10.1039/d3ya00378g

metal oxides/hydroxides[27,28] have been highly explored as supercapacitor materials. Among these materials, CPs have properties like tunable porosity, extensive surface area, and their flexibility to host a number of guest molecules and are attractive materials to be utilized for supercapacitor application. Moreover, their synthetic procedure also involves straightforward reaction pathways. Their properties can be tailored for a specific application by controlling the synthesized CP's size, shape, and composition. Constructing CPs with mixed linkers to produce 2D layered or 3D scaffolds is attractive due to their extensive use in the fields of energy or gas storage, sensing, and catalysis.[29–32]

The performance of CPs for supercapacitor applications can be enhanced using several strategies, including selecting the electrolyte since cations possessing a high charge density can increase the capacitance. However, the working potential window depends on the choice of electrolyte; the higher the cations' redox potential, the greater the potential window will be.[33,34] So, the choice of electrolyte becomes vital for the supercapacitor application. Many elements need to be examined, including conductivity, stability under the same working circumstances, mobility of the ions, viscosity, *etc.*[35] Each electrolyte has its own strength and weakness. Among liquid electrolytes, which are most often used for energy storage applications, organic and ionic electrolytes possess a wide range of working potential windows, which results in a high energy density value. The low conductivity and highly viscous nature show moderate capacitance and poor performance.[36] In contrast, aqueous electrolytes are inexpensive and environmentally safe. They have high ionic conductivity, low viscosity and exhibit good charge propagation with high performance.[37,38]

Recent studies have focused on exploring the potential of cobalt-based conductive polymers (CPs) for energy storage purposes, highlighting their unique structural and electrical characteristics. Recently, Shao *et al.*[39] prepared nanorod-shaped Co-MOFs synthesized using a solvothermal method, and they demonstrated notable electrochemical properties. They showed a specific capacitance (C_s) of 414.5 F g^{-1} at 0.5 A g^{-1} in a 3 M KOH electrolyte, while maintaining an impressive retention rate of 113% for up to 30 000 cycles. With an ASC device, it provides an energy density of 12.0 W h Kg^{-1} accompanied by a power density of 258.1 W Kg^{-1}. In another report, Kang *et al.*[40] described C_s of 726 F g^{-1} using a Ni-MOF, which exhibited 94.6% cyclic stability over 1000 cycles and displayed an energy density of 16.5 W h Kg^{-1}. Ma *et al.*[41] presented a Ni/Co based nanoscale coordination polymer (nCP) with a C_s of 1160.2 F g^{-1}, and it retained 66% capacitance over 7000 cycles. Hong *et al.*[42] synthesized a Ni–Co/graphene oxide composite *via* a one-pot solvothermal reaction, which exhibited a capacitance retention rate of 99.6% after 300 cycles and the observed C_s is 447.2 F g^{-1}. Moreover, various studies were performed to understand the effect of electrolytic cations on supercapacitor application to escalate the material's performance. In this regard, Houpt *et al.*[43] synthesized a composite of CNT-ZIF-MoS$_2$ as an electrode material and explored its electrochemical kinetics using LiCl, NaOH, KCl, and KOH electrolytes.

The composite exhibits the highest efficiency in KOH electrolytes. Moreover, Kumar *et al.*[44] developed a binary metal sulfide, denoted as CNS$_{0.15}$, and its efficacy was investigated across three different electrolytes: NaOH, KOH, and LiOH. Among these, it demonstrated superior performance, specifically in the NaOH electrolyte, exhibiting optimal efficiency. In our recent findings, we have observed a similar trend in a nickel-based polymer (Ni-CP),[45] where the highest capacitance was observed in NaOH electrolyte compared to other electrolytes.

In this report, we have synthesized a **Co-CP** employing a slow diffusion method which is well characterized using various techniques, including SC-XRD, PXRD, FT-IR, SEM, *etc.* The synthesized **Co-CP** used for the supercapacitor displayed a specific capacitance of 1092 F g^{-1} at 1.5 A g^{-1} while maintaining an excellent capacitance retention of 98% even after 6500 GCD cycles. Furthermore, to evaluate the kinetic effect of electrolytic cations, a thorough study was carried out using 1 M lithium hydroxide, sodium hydroxide and potassium hydroxide. The superior efficiency of **Co-CP** in NaOH electrolyte can be attributed to the synergistic impact of hydrated ionic radii and the ionic radii of cations. The straightforward synthetic approach at room temperature, simple electrode fabrication techniques, and additive and binder-free approach make it ideal for supercapacitor applications. In addition, an asymmetric (ASC) device was constructed, utilizing **Co-CP** and activated carbon as the positive and negative electrodes, respectively. This combination resulted in an impressive energy density of 17 W h Kg^{-1} and a power density of 1200 W Kg^{-1}. This study presents a straightforward synthetic route for **Co-CP**, offering a promising candidate for future energy storage applications.

Results and discussion

The room temperature assisted synthesis of **Co-CP** involved a mixed ligand strategy with 5-hydroxyisophthalic acid and DABCO reacting with Co(NO$_3$)$_2$·6H$_2$O under a slow diffusion process in a DMF/methanol buffer system (Scheme 1). The rose-pink colored crystals of **Co-CP** show a two-dimensional layered structure, where the DABCO molecule acts as a pillared ligand.

Crystal structure analysis

The monoclinic crystal system of **Co-CP** crystallizes in the $P_{21/m}$ space group. As shown in Fig. 1a, the Co(II) is coordinated by two 5-hydroxyisophthalic acid molecules, two DABCO molecules, and one methanol molecule. All the crystallographic data are compiled in Table 1. From Fig. 1b, the molecular unit of **Co-CP** represents the coordination mode of the Co(II) ion, where each Co(II) ion has an O$_4$N$_2$ coordination environment and forms a distorted octahedral geometry (Fig. S1a, ESI†). The coordination of three oxygen atoms from two 5-hydroxyisophthalic acid molecules, two nitrogen atoms from two DABCO molecules, and one oxygen atom from the coordinated methanol molecule (Fig. 1b) makes a distorted octahedral geometry around the Co(II) ion. The SCXRD analysis demonstrates that the 5-hydroxyisophthalic acid molecule shows ((κ1)-(κ1))-μ_2 and ((κ1)-(κ0))-μ_2 coordination
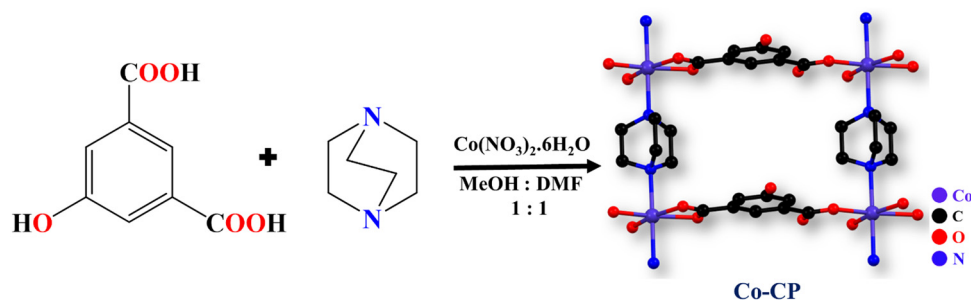
Scheme 1 Schematic for the synthesis of **Co-CP**.

modes (Fig. S1b, ESI†). The non-coordinated O atom of the –COO⁻ group participates in the H bonding interaction. The Co–O bond lengths were found to be in the 2.050(3) to 2.186(3) Å range; however, the Co–N bond distance is 2.272(2) Å. Table S1 (ESI†) includes a list of the additional significant bond distances (Å) and bond angles (°) of **Co-CP**. From Fig. S1c (ESI†), it is observed that the Co(II) ion extended in one dimensional layer along the *b*-axis by coordination of the carboxylate group of 5-hydroxyisophthalic acid in monodentate and bidentate modes. Additionally, as shown in Fig. 1c and d, the 1D chains are pillared *via* the DABCO molecule to form a two-dimensional (2D) network with square channels along the *b*-axis. The coordinated methanol molecule of one 2D framework and the O atom of the –COO⁻ group of the 5-hydroxyisophthalic acid from another 2D framework are further coupled by hydrogen bonding interactions (Fig. S2, ESI†), forming a 2D layered structure. The porous nature of **Co-CP** is seen in the space fill model (Fig. 1d).

Characterization of Co-CP

To authenticate that the bulk material obtained for **Co-CP** was phase pure and crystalline, we have recorded the Powder X-ray Diffraction (PXRD) spectrum of the material (Fig. 2a).

The experimental and simulated PXRD patterns demonstrate consistency in terms of relative intensities and resolutions obtained from the reflections. However, it is important to acknowledge a slight disparity in the intensities of the peaks.[46] Importantly, all the significant peaks mimic the simulated pattern. From Fig. 2a, it was observed that the experimental pattern resembles the simulated **Co-CP** pattern, confirming that the high-phase pure material and the sharp peaks represent the material's crystallinity.

Moreover, to further confirm the bonding interactions between the metal atom and the ligand moiety, the FT-IR spectrum were recorded within 4000–400 cm⁻¹ (Fig. 2b). The broad band observed at 3073 cm⁻¹ represents the ν_{OH} from the associated water molecule. The band observed at 1660 cm⁻¹ and 1373 cm⁻¹ confirms the asymmetric $\nu_{as(COO^-)}$ and symmetric $\nu_{s(COO^-)}$ carboxylate groups.[47] The peaks at 1546 cm⁻¹ signify the phenyl ring stretching vibrational mode.[48] The distinct peak observed at 780 cm⁻¹ was attributed to the Co–O stretching frequency.[49] Moreover, the peaks at 2971, 1280, 1100, and 1050 cm⁻¹ depict the characteristics of ν(C–H), ν(C–N), ν(C–C), and ν(C–N) stretching frequencies, respectively.[50]

To understand the thermal stability of the material we also performed thermogravimetric analysis (TGA) for **Co-CP** (Fig. 2c).
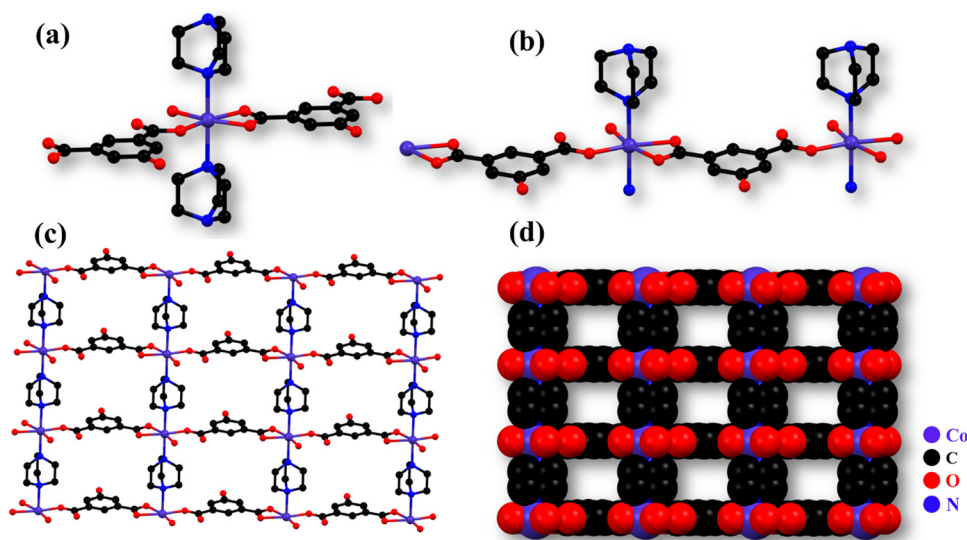

Fig. 1 (a) Coordination environment around the Co(II) ion, (b) molecular unit, (c) 2D layered structure, and (d) space fill model of **Co-CP** view along the *b*-axis (hydrogen atoms are omitted for clarity).

Table 1 Crystallographic information of **Co-CP**

Empirical formula	$C_9H_{13.50}Co_{0.50}N_{1.50}O_{3.50}$
Formula weight	228.18
Temperature	293(2) K
Wavelength	0.71073 Å
Space group	Monoclinic, $P2_{1/m}$
a	10.3390(4) Å
b	7.1811(3) Å
c	13.8946(6) Å
α	90°
β	91.287(3)°
γ	90°
Volume	1031.35(7) Å^3
Z	4
Density	1.470 mg m^{-3}
Absorption coefficient	0.877 mm^{-1}
$F(000)$	478
Crystal size	0.330 × 0.260 × 0.210 mm
Theta range for data collection	2.933 to 29.058°
Limiting indices	$-14 \Leftarrow h \Leftarrow 13, -8 \Leftarrow k \Leftarrow 9,$ $-17 \Leftarrow l \Leftarrow 18$
Reflections collected/unique	10592/2712 [R(int) = 0.0611]
Absorption correction	Semi-empirical from equivalents
Max. and min. transmission	1.00000 and 0.71696
Refinement method	Full-matrix least-squares on F^2
Data/restraints/parameters	2712/0/169
Goodness-of-fit on F^2	1.089
Final R indices [$I > 2\text{sigma}(I)$]	$R_1 = 0.0529$, w$R_2 = 0.1288$
R indices (all data)	$R_1 = 0.0754$, w$R_2 = 0.1432$
Largest diff. peak and hole	0.567 and -0.396 e Å^{-3}
CCDC No.	2285196

From Fig. 2c it is observed that the degradation of **Co-CP** occurs in two major steps, at first, the degradation starts from 100 °C signifying the removal of coordinated methanol molecules.

Beyond that the second steps represent the degradation associated DMF molecule in the moiety up to 200 °C. After that gradual degradation occurs representing breakdown of the benzene ring up to a temperature of 350 °C. At last, the complete degradation of the moiety observed in the temperature starting from 450 °C. Therefore, the high thermal stability of the **Co-CP** signifies its possibility for electrochemical energy storage at high temperatures.

Studying surface morphology is essential to understanding the ion transportation mechanism. In this context, scanning electron microscope (SEM) images were recorded at various magnifications using Au coating and Al as a substrate for **Co-CP** (Fig. 2d and e). The observed images demonstrate sheet or plate-like morphology. The disoriented structural morphology with uneven edges may favour a more active site for reaction and could give better transmission possibilities for ions for electrochemical reactions.[51] The observed average l/d ratio for **Co-CP** is 1.908, which may induce more open sites for electrolytic ions to take part in electrochemical reactions. Moreover, the excellent results of **Co-CP** towards the electrochemical supercapacitor application may be attributed due to the redox active Co(II) metal center and high interspaces within the molecules for high transmission possibilities of ions. Later on, energy dispersive spectroscopy (EDS) was also studied to further authenticate the PXRD results. The observed wt% for Co, N, O, and C are 0.6, 9.4, 34.8, and 46.8, respectively (Fig. 2f). Due to the gold (Au) coating and use of aluminium (Al) as a substrate, the peaks for Au and Al were observed in EDS.
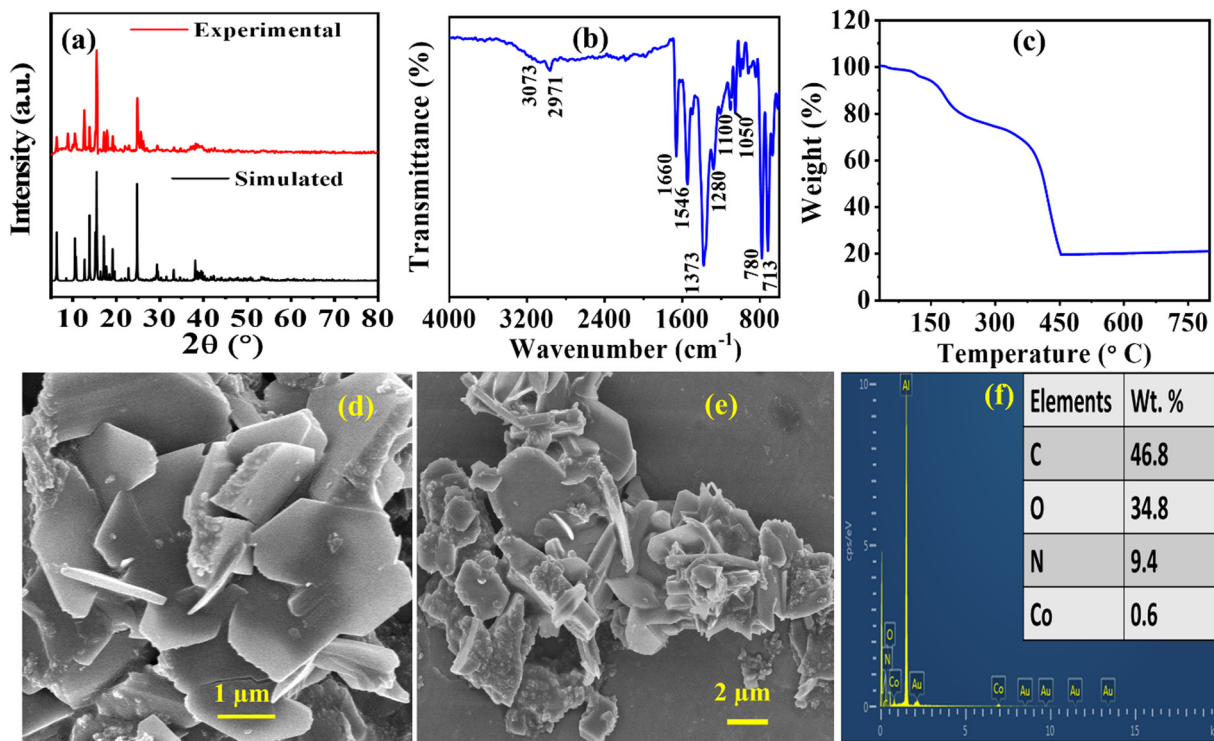

Fig. 2 (a) X-ray diffraction spectrum, (b) Fourier transform-infrared spectrum, (c) TGA spectra, (d) and (e) FE–SEM images, and (f) elemental compositions of **Co-CP**.

In the context of electrochemical supercapacitor applications, surface area and pore size become crucial parameters. To determine these, Brunauer–Emmett–Teller (BET) analysis was conducted at 77 K and the results are presented in Fig. S3 (ESI†). From the crystal structure of **Co-CP**, it is seen that both the COO^- groups of 5-hydroxyisophthalic acid are connected with the metal center and the N atom of the DABCO linker is also occupied within the metal center. Therefore, the functional groups available to interact with the adsorbed N_2 molecule are limited. Consequently, the interaction between adsorbate-adsorbent is weak, and adsorbed molecules are clustered around the material's surface.[52,53] So, in the case of **Co-CP**, we observed a type III BET isotherm. The observed BET analysis reveals a type III isotherm pattern, indicating the characteristic behavior of the material. The BET surface area of **Co-CP** is found to be 169.613 $m^2 g^{-1}$ with a pore size of 3.829 nm. The observed value of the surface area is comparable to various MOF and coordination polymer-based literature with excellent supercapacitor applications.[54–56] The observed surface area offers an increased number of sites for electrochemical reactions, enhancing the potential for efficient energy storage. Additionally, the presence of a suitable pore diameter facilitates improved ion transportation, further enhancing the performance of the system.

Electrochemical efficiency evaluation

CV curves were recorded within the potential window of 0 to 0.54 V at various scan rates to determine the electrochemical efficiency of the prepared **Co-CP** modified carbon cloth electrode. To assess the impact of different electrolytic cations (Na^+, K^+, Li^+), the efficiency of the active material was examined in three distinct aqueous electrolytes: NaOH, KOH, and LiOH (Fig. S4–S6, ESI†). From the CV curve of **Co-CP** in 1 M (NaOH, KOH, LiOH), it is clearly observed that the area of the CV is ascending in the order of NaOH > KOH > LiOH (Fig. 3a). The results obtained from the comparative CV curve define the most suitable electrolyte is NaOH, and therefore it delivers the maximum efficiency. The effect of electrolytic cations on the electrochemical properties can be understood by considering the hydrated ionic radii and ionic sizes as determining factors. The hydrated ionic radii were ascending in the order of K^+ (0.3 nm) < Na^+ (0.4 nm) < Li^+ (0.6 nm).[57] The increment of hydrated ionic radii reduces the possibility of transmission of ions from the electrolyte solution to the active material. Thus, we observe the lowest efficiency in LiOH compared to NaOH and KOH. On the other hand, the ionic sizes of cation also comes into consideration for NaOH and KOH. As the K^+ (0.138 nm) ion has a large ionic size relative to Na^+ (0.102 nm),[57] the diffusion rate of K^+ ion towards the electrode decreases as compared to Na^+. Consequently, the combined effect of hydrated ionic radii and ionic sizes leads to the superior efficiency of NaOH compared to KOH. The specific capacitance values were calculated from GCD using eqn (S1) (ESI†) for all three electrolytes at 1.5 A g^{-1}. NaOH delivers the highest specific capacitance values of 706 F g^{-1} over 625 F g^{-1} for KOH and 420 F g^{-1} for LiOH. The values of specific capacitance in all three electrolytes at different current densities are included in Table S2 (ESI†).

As **Co-CP** delivers the maximum performance in 1 M NaOH, therefore the electrolyte concentration of NaOH further varied
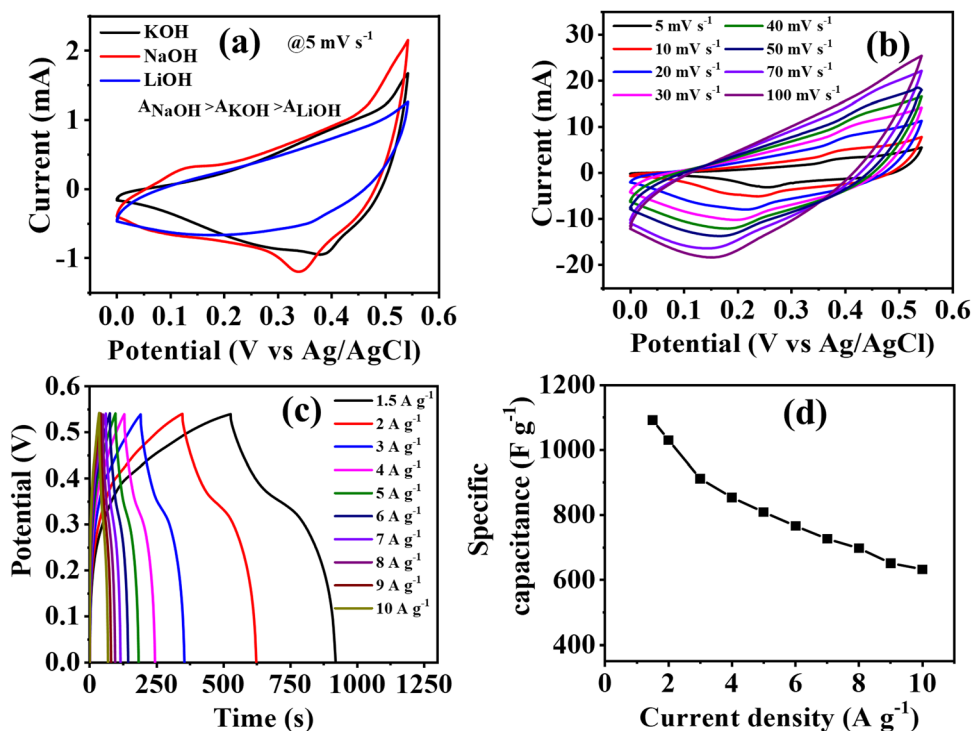

Fig. 3 (a) Comparative CV curve for different electrolytes, (b) CV at various scan rates, (c) GCD at different current densities, and (d) specific capacitance *vs.* current density for **Co-CP** in 7 M NaOH.

to 1 M, 3 M, 5 M, and 7 M (Fig. S4, S7, S8, ESI† and Fig. 3). As the concentration of electrolytes increases, the specific capacitance also improves, and 7 M NaOH delivers the highest capacitance values. As the concentration varies from 1 M to 7 M NaOH, a high charge–discharge time is observed, but the electrochemical measurements are challenging beyond this concertation. At higher electrolytic concentrations, the ionic activity reduces, and the hydration of water diminishes, finally minimizes ionic mobility.[57] As 7 M NaOH delivered the highest efficiency in the detailed investigation of electrochemical properties of **Co-CP** through the CV, GCD techniques are included in Fig. 3b and c. From the CV curve in Fig. 3b, with different scan rates from 5 mV s^{-1} to 100 mV s^{-1}, the distinct peak of the Co^{2+}/Co^{3+} redox couple is clearly visible. The observed CV curve shows the pseudocapacitive nature of **Co-CP**. With an increase of scan rates, the redox couple shifts towards more positive and negative regions due to the increase of ionic mobility at high scan rates. A similar trend is also observed when the concertation of electrolytes varied from 1 M to 7 M NaOH. The difference in the peak potential *i.e.*, $\Delta E_p = E_{pa} - E_{pc}$ are 120, 140, 150, 200, 230, 260, 280, and 300 mV for 5, 10, 20, 30, 40, 50, 70, and 100 mV s^{-1} (Fig. 3b). This behavior can illustrate better reaction kinetics at the electrode/electrolyte junction due to easy ionic and electronic transportation.[45] The reversible OH$^-$ intercalation reaction occurring through the faradaic process can provide an explanation for the pseudocapacitive behavior observed in **Co-CP**.

$$Co(OH)_2(C_9H_{12.50}N_{1.50}O_{2.50})_2 + OH^\bullet \rightleftharpoons$$
$$CoO(OH)(C_9H_{12.50}N_{1.50}O_{2.50})_2 + H_2O$$
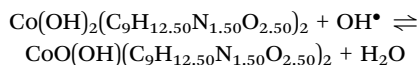
Furthermore, the GCD curve was recorded for **Co-CP** at various current densities from 1.5 A g^{-1} to 10 A g^{-1} (7 M NaOH) (Fig. 3c) and specific capacitance was obtained by using eqn (S1) (ESI†) from the GCD curve (Fig. 3d). The GCD pattern exhibits a typical nonlinear behavior representing the pseudocapacitive nature of the material, these characteristics resemble very well with the CV plot. The GCD pattern represents the symmetrical nature for charging and discharging, suggesting higher Coulombic efficiency. The pseudocapacitive material delivers two distinct regions for GCD: (i) the sudden fall in potential represents the internal resistance offered by the

solutions, and (ii) the next decline of potential represents the capacitive nature of **Co-CP**.[58] **Co-CP** being the pseudocapacitive material, offered a specific capacitance of 1092 F g^{-1} at 1.5 A g^{-1} and this was maintained up to 633 F g^{-1} at 10 A g^{-1}, suggesting high-rate performance at a high current density. The decrease in the efficiency at high current density indicates that at low current densities, a high-rate performance is experienced because of the ohmic drop, but at high current density, the reaction kinetics become sluggish. At low current density, the electrolytic cation gets enough time to interact with the active site of the material, thus offering a high capacitance value. The highest specific capacitance was obtained at different NaOH concentrations.

Moreover, to find all the resistance parameters of **Co-CP** in 1 M (NaOH, KOH, and LiOH), the Nyquist plot was recorded within the frequency range of 0.1 to 10^5 Hz (Fig. 4a). The Nyquist plot is comprised of two distinct regions: (i) semi-circular loop at high-frequency region; the intercepts along the *x*-axis represents the solution resistance (R_s) representing all the resistance offered by the solutions, (ii) a vertical straight line in the low-frequency region, the slope of this line along the imaginary axis ($-Z''$) represents the charge transfer resistance.[59] Along with this two-resistance parameter, two capacitance parameters are also associated: (i) double layer capacitance (C_{dl}), representing of storage of charge at electrode/electrolyte junctions, and (ii) pseudo capacitance (C_p), signifying charge storage *via* a redox reaction. The Warburg impedance (W) in the low-frequency region was also found because of the linear diffusion. In redox reactions, high diffusion rate of electrolyte ions lead to the Warburg impedance.[59] The circuit fitting parameters for the Nyquist plots are tabulated in Table S3 (ESI†). The results obtained from CV and GCD analysis resemble well with the Nyquist plots, as **Co-CP** experiences the highest solutions resistance in 1 M LiOH (11.2 Ω), followed by 1 M KOH (8.6 Ω), and 1 M NaOH (7.45 Ω). The combined influence of hydrated ionic radii and ionic sizes of Li$^+$, K$^+$, and Na$^+$ illustrate well the solution resistance offered by the electrolyte ions. Another interesting parameter for the supercapacitor study is the cyclic stability of the materials. Here, we have studied the cyclic stability of **Co-CP** in 1 M (NaOH, KOH, and LiOH) up to 6500 cycles through continuous GCD cycles (Fig. 4b). The **Co-CP** shows excellent cyclic retention of 98%, 97%, and 96% respectively for NaOH, KOH, and LiOH after completion of 6500
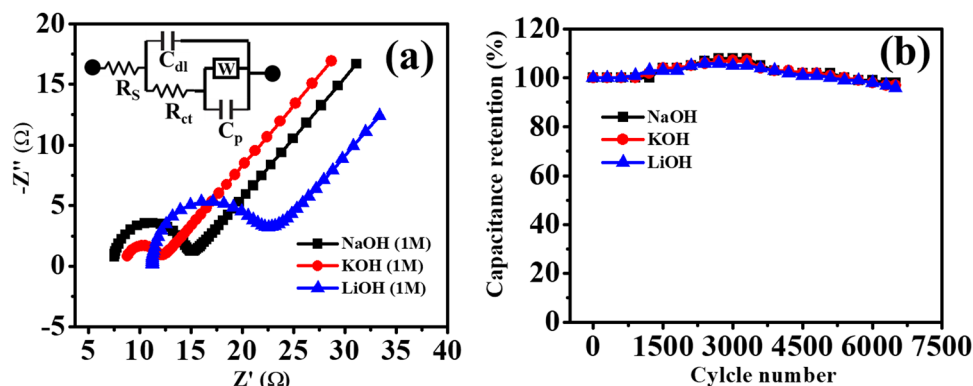

Fig. 4 (a) Nyquist plot, and (b) cyclic stability of **Co-CP** in 1 M NaOH, KOH, and LiOH.

GCD cycles. The high cyclic retention indicates the excellent stability of **Co-CP** throughout the continuous cycles of GCD. After the completion of a few hundred cycles, the retention value goes above 100%; this behavior is experienced due to the increase in the wettability of the material and activation of the material.[45,60] During this stage, the electrolyte ions traverse the interior surface in order to access the pores of the active materials.[61] As the cycling continues, the surface wettability of the material continues to improve. This enhanced wettability facilitates the ongoing diffusion of electrolyte ions throughout the electrode's microstructure, creating more efficient pathways to reach deeper particles within the material. This enhanced diffusion process contributes to an activation effect that persists throughout the electrochemical cycling. Consequently, this leads to an increase in capacitance as the cycling progresses.[62,63] The minute loss of capacitance value may occur due to the continuous intercalation and deintercalation process of electrolyte ions through the electrode surface which causes mechanical stress and reduces the capacitance value. To support the loss of minimum capacitance value after the cyclic stability measurement, the electrochemical active surface area (EASA) is measured before and after the cyclic stability analysis. Furthermore, detailed information regarding EASA calculation is provided in the ESI,† Fig. S12. The observed EASA of **Co-CP** before the measurement is 0.7 cm^2, which is reduced to 0.55 cm^2 after 6500 GCD cycles. The decrease in the EASA value favored the slight degradation of the cyclic retention value. Moreover, the morphology of **Co-CP** was also investigated after the completion of the stability test. It is evident from Fig. S13 (ESI†) that the plate or sheet-like surface morphology is intact even after obtaining the cyclic stability measurements, which suggests the high stability of **Co-CP**.

Study of asymmetric solid-state supercapacitor (ASC)

Furthermore, to validate the practical utility of **Co-CP**, an ASC device was fabricated with **Co-CP** as the positive electrode material and activated carbon as the negative electrode material.
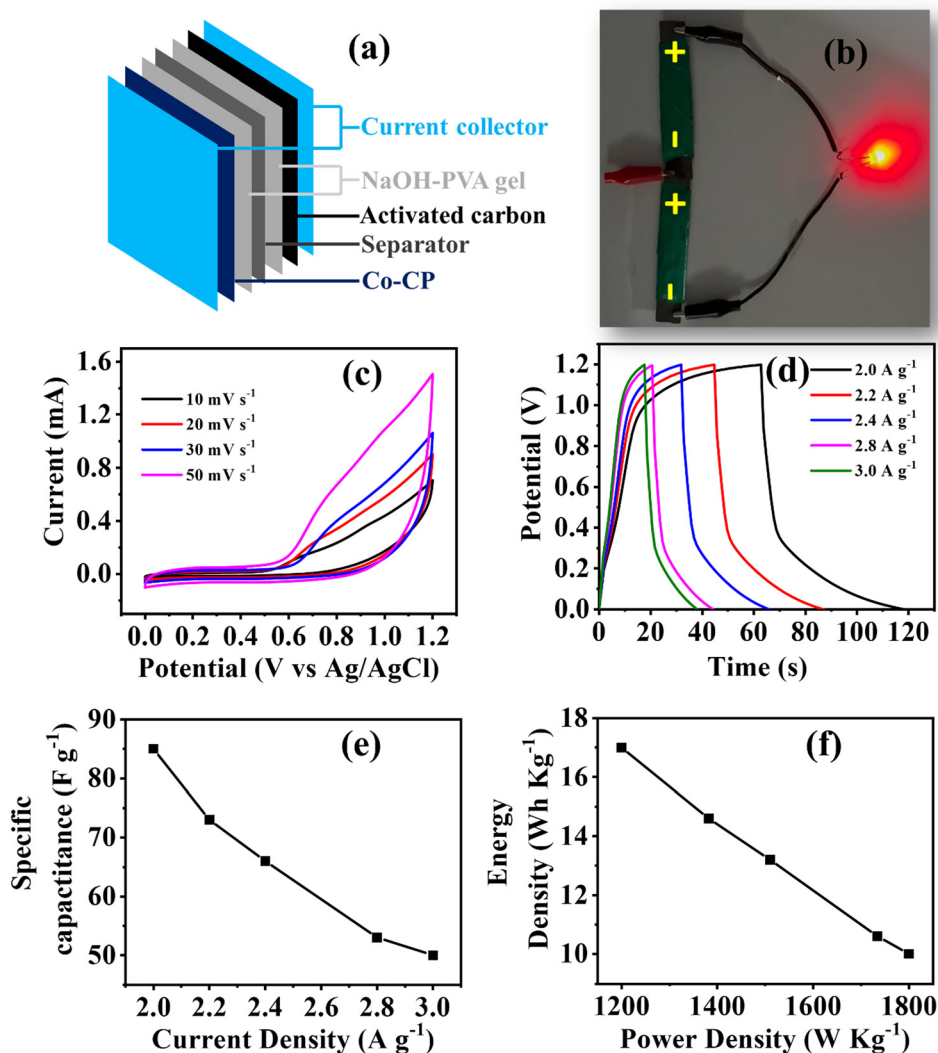

Fig. 5 (a) and (b) ASC device illustration, (c) CV at various scan rates, (d) GCD at different current densities, (e) specific capacitance *vs.* current density curve, and (f) Ragone plot of the **Co-CP** ASC device with NaOH-PVA gel.

Table 2 Coordination polymer, MOF, and MOF-derived materials for both three and two-electrode supercapacitor applications

| | | | | | | ASC device | | |
S. no.	Material	Electrolyte	Current density (A g^{-1})	Specific capacitance (F g^{-1})	Cyclic stability	Energy density (W h Kg^{-1})	Power density (W Kg^{-1})	Ref.
1	Co,N-doped CP	6 M KOH	1	330	98%, 3000 cycles	9.1	700	64
2	{Ni(TPTA)(1-4-bib)}-MOF	1 M KOH	0.5	227.1	90.8%, 2000 cycles	8.36	501.3	65
3	Co-MOF derived Co$_3$O$_4$	2 M KOH	1.3	226.1	89.9%, 20 000 cycles	0.092 mW h cm^{-3}	1.34 mW h cm^{-3}	66
4	Ni-MOF/rGO	6 M KOH	1	954	80.25%, 4000 cycles	17.13	750	67
5	Ni-MOF nanosheets	1 M KOH	1	1024.4	49%, 5000 cycles	13	—	68
6	Co-NTA	3 M KOH	1.4	395	96.5%, 5000 cycles	4.18 mW h cm^{-3}	231.2 mW h cm^{-3}	69
7	Ni–Co-MOF	3 M KOH	1	827.9	—	29.1	800	70
8	Co based film	1 M LiOH	0.6	206.7	98.5%, 1000 cycles	7.18	—	71
9	Zn(tbip) derived porous C	6 M KOH	0.5	369	96%, 2000 cycles	12.5	7200	72
10	Ni-CP	7 M KOH	3	802	95% after 5000 cycles	15	1137	45
11	Co-MOF	3 M KOH	0.5	414.5	113%, 20 000 cycles	12	258	47
12	rGO/ZIF-8	1 M KOH	1	336	96%, 10 000 cycles	11.7	500	73
13	Ni-BPDC/GO-3	6 M KOH	1	630	95.7%, 10 000 cycles	16.5	250	74
14	Ni-MOF	1 M KOH	1	1024	49.1%, 5000 cycles	14.6	400	68
15	Ni–C/Ni-BDC	6 M KOH	2	672	57%	17.8	350	75
16	**Co-CP**	**7 M NaOH**	**1.5**	**1092**	**98%, 6500 cycles**	**17**	**1200**	**This Work**

To assemble the device, at first carbon paper was used with the dimensions (1.5 cm × 4 cm) as a support for both the positive/negative electrode material. As we have studied the effect of three electrolytic cations, therefore to study the effect on the device system, we have prepared the gel from all three electrolytes (NaOH-PVA, KOH-PVA, and LiOH-PVA) for 4h at 350 K. The electrodes were immersed in the gel for a certain brief duration and then stacked together, with cellulose paper (0.45 Millipore) acting as a spacer, to form a sandwich structure (Fig. 5a). The fabricated device was than charged with an AC adaptor for 30s and able to make a LED bulb (∼1.8 V) glow for a few seconds (Fig. 5b). To evaluate the device efficiency the electrochemical set up was used for CV, GCD (Fig. 5c–e and Fig. S9–S10, ESI†) and EIS measurements (Fig. S11, ESI†). The specific capacitance observed for the device (NaOH-PVA gel) delivers a specific capacitance of 85 F g^{-1} at 2 A g^{-1}. This value is higher than that of the KOH-PVA gel device (64 F g^{-1}) and LiOH-PVA gel device (47 F g^{-1}) (Table S4, ESI†). From the GCD results, a similar trend was observed in the case of the two electrode system with that of three electrode systems. Moreover, the EIS was recorded for the NaOH-PVA gel device, and the circuit fitting parameters were tabled in Table S5 (ESI†). Furthermore, the Ragone plot is shown in Fig. 5f; the observed energy density 17 W h Kg^{-1} with a power density of 1200 W Kg^{-1} value of **Co-CP** (NaOH-PVA gel) is found to be comparable to many coordination polymer-based, MOF or MOF derived materials as illustrated in Table 2.

Conclusions

In summary, a cobalt-based two-dimensional coordination polymer was synthesized using a simple slow diffusion technique. The **Co-CP** structure is authenticated through SC-XRD followed by PXRD, FT-IR, and SEM analysis. The two-dimensional **Co-CP** is utilized as an active material in supercapacitor applications, exhibiting a specific capacitance of 1092 F g^{-1} at 1.5 A g^{-1} in 7 M NaOH. Subsequently, the influence of different electrolytic cations (Na$^+$, K$^+$, Li$^+$) was investigated. The **Co-CP** demonstrates

superior efficiency in NaOH compared to KOH and LiOH, attributed to the combined impact of hydrated ionic radii and ionic radii. To validate the electrolytic effect further, ASC devices were fabricated using three different gel systems (NaOH-PVA, KOH-PVA, and LiOH-PVA). A similar trend of the electrochemical results was experienced for the devices. The fabricated device, however, delivers an energy density of 17 W h Kg^{-1} with a power density of 1200 W Kg^{-1} in the NaOH-PVA gel system. Thus, this study offers a straightforward synthetic pathway along with a convenient fabrication method for **Co-CP**, making it promising for supercapacitor applications.

Conflicts of interest

There are no conflicts to declare.

Acknowledgements

References

1 F. Boorboor Ajdari, E. Kowsari, M. Niknam Shahrak, A. Ehsani, Z. Kiaei, H. Torkzaban, M. Ershadi, S. Kholghi Eshkalak, V. Haddadi-Asl, A. Chinnappan and S. Ramakrishna, *Coord. Chem. Rev.*, 2020, **422**, 213441.

2 X. Luo, J. Wang, M. Dooner and J. Clarke, *Appl. Energy*, 2015, **137**, 511–536.

3 V. Kumar, P. Kumar, R. Deka, Z. Abbas and S. M. Mobin, *Chem. Rec.*, 2022, **22**, e202200067.

4   A. González, E. Goikolea, J. A. Barrena and R. Mysyk, *Renewable Sustainable Energy Rev.*, 2016, **58**, 1189–1206.

5   J. Libich, J. Máca, J. Vondrák, O. Čech and M. Sedlaříková, *J. Energy Storage*, 2018, **17**, 224–227.

6   R. Kumar, S. Naz Ansari, R. Deka, P. Kumar, M. Saraf and S. M. Mobin, *Chem. – Eur. J.*, 2021, **27**, 13669–13698.

7   J. R. Miller and P. Simon, *Science*, 2008, **321**, 651–652.

8   A. González, E. Goikolea, J. A. Barrena and R. Mysyk, *Renewable Sustainable Energy Rev.*, 2016, **58**, 1189–1206.

9   X. Li, X. Xiao, Q. Li, J. Wei, H. Xue and H. Pang, *Inorg. Chem. Front.*, 2018, **5**, 11–28.

10 R. Kötz and M. Carlen, *Electrochim. Acta*, 2000, **45**, 2483–2498.

11 N. R. Tummuru, M. K. Mishra and S. Srinivas, *IEEE Trans. Ind. Electron.*, 2015, **62**, 7728–7737.

12 M. Zandi, A. Payman, J.-P. Martin, S. Pierfederici, B. Davat and F. Meibody-Tabar, *IEEE Trans. Veh. Technol.*, 2011, **60**, 433–443.

13 B. Dunn, H. Kamath and J.-M. Tarascon, *Science*, 2011, **334**, 928–935.

14 M. V. Kiamahalleh, S. H. S. Zein, G. Najafpour, S. A. Sata and S. Buniran, *NANO*, 2012, **07**, 1230002.

15 Q. Du, M. Zheng, L. Zhang, Y. Wang, J. Chen, L. Xue, W. Dai, G. Ji and J. Cao, *Electrochim. Acta*, 2010, **55**, 3897–3903.

16 L. L. Zhang, R. Zhou and X. S. Zhao, *J. Mater. Chem.*, 2010, **20**, 5983.

17 R. Deka, D. D. Mal and S. M. Mobin, *Dalton Trans.*, 2023, **52**, 8204–8210.

18 N. Parveen and M. H. Cho, *Sci. Rep.*, 2016, **6**, 27318.

19 S. K. Meher and G. R. Rao, *J. Phys. Chem. C*, 2011, **115**, 15646–15654.

20 G. Chen, X. Li, L. Zhang, N. Li, T. Y. Ma and Z. Liu, *Adv. Mater.*, 2016, **28**, 7680–7687.

21 B. Anasori, M. R. Lukatskaya and Y. Gogotsi, *Nat. Rev. Mater.*, 2017, **2**, 16098.

22 K. Nabeela, R. Deka, Z. Abbas, P. Kumar, M. Saraf and S. M. Mobin, *Cryst. Growth Des.*, 2023, **23**(5), 3057–3078.

23 S. Chandra, D. Roy Chowdhury, M. Addicoat, T. Heine, A. Paul and R. Banerjee, *Chem. Mater.*, 2017, **29**, 2074–2080.

24 H. H. Nersisyan, B. U. Yoo, S. H. Joo, T. H. Lee, K.-H. Lee and J.-H. Lee, *J. Chem. Eng.*, 2015, **281**, 218–226.

25 D. Wu, K. Cao, F. Wang, H. Wang, Z. Gao, F. Xu, Y. Guo and K. Jiang, *J. Chem. Eng.*, 2015, **280**, 441–447.

26 W. Li, L. Sun, J. Qi, P. Jarillo-Herrero, M. Dincǎ and J. Li, *Chem. Sci.*, 2017, **8**, 2859–2867.

27 B. Zhao, D. Chen, X. Xiong, B. Song, R. Hu, Q. Zhang, B. H. Rainwater, G. H. Waller, D. Zhen, Y. Ding, Y. Chen, C. Qu, D. Dang, C.-P. Wong and M. Liu, *Energy Storage Mater.*, 2017, **7**, 32–39.

28 X. Cai, X. Shen, L. Ma, Z. Ji, C. Xu and A. Yuan, *J. Chem. Eng.*, 2015, **268**, 251–259.

29 L. Yu, X. Wang, M. Cheng, H. Rong, Y. Song and Q. Liu, *Cryst. Growth Des.*, 2018, **18**, 280–285.

30 J.-R. Li, J. Sculley and H.-C. Zhou, *Chem. Rev.*, 2012, **112**, 869–932.

31 R. Rajak, M. Saraf, S. K. Verma, R. Kumar and S. M. Mobin, *Inorg. Chem.*, 2019, **58**, 16065–16074.

32 H.-Y. Wang, J. Su, J.-P. Ma, F. Yu, C. F. Leong, D. M. D'Alessandro, M. Kurmoo and J.-L. Zuo, *Inorg. Chem.*, 2019, **58**, 8657–8664.

33 T. Liu, W. G. Pell and B. E. Conway, *Electrochim. Acta*, 1997, **42**, 3541–3552.

34 B. E. Conway, W. G. Pell and T.-C. Liu, *J. Power Sources*, 1997, **65**, 53–59.

35 D.-W. Wang, F. Li, M. Liu, G. Q. Lu and H.-M. Cheng, *Angew. Chem., Int. Ed.*, 2008, **120**, 379–382.

36 C. Zhong, Y. Deng, W. Hu, J. Qiao, L. Zhang and J. Zhang, *Chem. Soc. Rev.*, 2015, **44**, 7484–7539.

37 X. Peng, H. Liu, Q. Yin, J. Wu, P. Chen, G. Zhang, G. Liu, C. Wu and Y. Xie, *Nat. Commun.*, 2016, **7**, 11782.

38 S. Lehtimäki, A. Railanmaa, J. Keskinen, M. Kujala, S. Tuukkanen and D. Lupo, *Sci. Rep.*, 2017, **7**, 46001.

39 D. Shao, L. Wang, B. Lu, J. Guo, S. Zhang and Y. Lu, *J. Electroanal. Chem.*, 2019, **847**, 113188.

40 L. Kang, S.-X. Sun, L.-B. Kong, J.-W. Lang and Y.-C. Luo, *Chin. Chem. Lett.*, 2014, **25**, 957–961.

41 Q. Ma, F. Cui, J. Zhang, Y. Yan and T. Cui, *ACS Appl. Energy Mater.*, 2022, **5**, 12165–12173.

42 J. Hong, S.-J. Park and S. Kim, *Electrochim. Acta*, 2019, **311**, 62–71.

43 D. Houpt, J. Ji, D. Yang and J. H. Choi, *ACS Appl. Nano Mater.*, 2022, **5**, 1491–1499.

44 V. Kumar and H. S. Panda, *Mater. Chem. Phys.*, 2021, **272**, 125042.

45 R. Deka, V. Kumar, R. Rajak and S. M. Mobin, *Sustainable Energy Fuels*, 2022, **6**, 3014–3024.

46 D. Frahm, M. Fischer, F. Hoffmann and M. Fröba, *Inorg. Chem.*, 2011, **50**, 11055–11063.

47 D. Shao, L. Wang, B. Lu, J. Guo, S. Zhang and Y. Lu, *J. Electroanal. Chem.*, 2019, **847**, 113188.

48 Y. Wang, J.-X. Ma, Y. Zhang, N. Xu and X.-L. Wang, *Cryst. Growth Des.*, 2021, **21**, 4390–4397.

49 X. Hu, H. Wang, S. Qi, Z. Su, J. Wang, K. Chen, S. Li, X. Huang, S. Luo and A. Xie, *Ionics*, 2022, **28**, 813–821.

50 R. Rajak, M. Saraf, S. K. Verma, R. Kumar and S. M. Mobin, *Inorg. Chem.*, 2019, **58**, 16065–16074.

51 S. Gao, Y. Sui, F. Wei, J. Qi, Q. Meng and Y. He, *J. Mater. Sci.*, 2018, **53**, 6807–6818.

52 R. Rajak, M. Saraf and S. M. Mobin, *Inorg. Chem.*, 2020, **59**, 1642–1652.

53 F. Ambroz, T. J. Macdonald, V. Martis and I. P. Parkin, *Small Methods*, 2018, **2**, 1800173.

54 X. Liu, C. Shi, C. Zhai, M. Cheng, Q. Liu and G. Wang, *ACS Appl. Mater. Interfaces*, 2016, **8**, 4585–4591.

55 R. Rajak, M. Saraf, A. Mohammad and S. M. Mobin, *J. Mater. Chem. A*, 2017, **5**, 17998–18011.

56 R. Deka, R. Rajak, V. Kumar and S. M. Mobin, *Inorg. Chem.*, 2023, **62**, 3084–3094.

57 V. Kumar and H. S. Panda, *Mater. Chem. Phys.*, 2021, **272**, 125042.

58 A. Shokry, M. Karim, M. Khalil, S. Ebrahim and J. El Nady, *Sci. Rep.*, 2022, **12**, 11278.

59 H. S. Tripathi, A. Dutta and T. P. Sinha, *Electrochim. Acta*, 2022, **421**, 140505.

60 X. Y. Liu, Y. Q. Gao and G. W. Yang, *Nanoscale*, 2016, **8**, 4227–4235.

61 A. Barua, P. Mehra and A. Paul, *ACS Appl. Energy Mater.*, 2021, **4**, 14249–14259.

62 M. Ramadan, A. M. Abdellah, S. G. Mohamed and N. K. Allam, *Sci. Rep.*, 2018, **8**, 7988.

63 T. Wang, Z. Peng, Y. Wang, J. Tang and G. Zheng, *Sci. Rep.*, 2013, **3**, 2693.

64 A. K. Díaz-Duran, G. Montiel, F. A. Viva and F. Roncaroli, *Electrochim. Acta*, 2019, **299**, 987–998.

65 Z. Zhang, L. Gao, J. Zhang, X. Niu and T. Hu, *J. Solid State Chem.*, 2020, **292**, 121711.

66 Y. Tao, Y. Wu, H. Chen, W. Chen, J. Wang, Y. Tong, G. Pei, Z. Shen and C. Guan, *J. Chem. Eng.*, 2020, **396**, 125364.

67 Y. Zhong, X. Cao, L. Ying, L. Cui, C. Barrow, W. Yang and J. Liu, *J. Colloid Interface Sci.*, 2020, **561**, 265–274.

68 M. Gu, M. Wu, S.-C. Wang, C. Chen, D. Xiong and F.-Y. Yi, *Electrochim. Acta*, 2020, **343**, 135617.

69 Y. Yan, P. Gu, S. Zheng, M. Zheng, H. Pang and H. Xue, *J. Mater. Chem. A*, 2016, **4**, 19078–19085.

70 L. Quan, T. Liu, M. Yi, Q. Chen, D. Cai and H. Zhan, *Electrochim. Acta*, 2018, **281**, 109–116.

71 D. Y. Lee, S. J. Yoon, N. K. Shrestha, S.-H. Lee, H. Ahn and S.-H. Han, *Microporous Mesoporous Mater.*, 2012, **153**, 163–165.

72 X.-M. Cao, Z.-J. Sun, S.-Y. Zhao, B. Wang and Z.-B. Han, *Mater. Chem. Front.*, 2018, **2**, 1692–1699.

73 E. Samuel, B. Joshi, C. Park, A. Aldalbahi, M. Rahaman and S. S. Yoon, *Electrochim. Acta*, 2020, **362**, 137154.

74 F. He, N. Yang, K. Li, X. Wang, S. Cong, L. Zhang, S. Xiong and A. Zhou, *J. Mater. Res.*, 2020, **35**, 1439–1450.

75 Z. Bai, S. Liu, P. Chen, G. Cheng, G. Wu, H. Li and Y. Liu, *Nanotechnology*, 2020, **31**, 305705.